CHALMERS | UNIVERSITY OF GOTHENBURG

PREPRINT 2011:22

Reconstruction of dielectrics in a symmetric structure via adaptive algorithm with backscattering data

LARISA BEILINA
MARTE P. HATLO ANDRESEN
HARALD E. KROGSTAD

Department of Mathematical Sciences
Division of Mathematics
CHALMERS UNIVERSITY OF TECHNOLOGY
UNIVERSITY OF GOTHENBURG
Gothenburg Sweden 2011

Preprint 2011:22

Reconstruction of dielectrics in a symmetric structure via adaptive algorithm with backscattering data

Larisa Beilina, Marte P. Hatlo Andresen,
Harald E. Krogstad

Department of Mathematical Sciences
Division of Mathematics
Chalmers University of Technology and University of Gothenburg
SE-412 96 Gothenburg, Sweden
Gothenburg, October 2011

Preprint 2011:22
ISSN 1652-9715

Matematiska vetenskaper
Göteborg 2011

Reconstruction of dielectrics in a symmetric structure via adaptive algorithm with backscattering data

Larisa Beilina * Marte P. Hatlo Andresen † Harald E. Krogstad ‡

October 7, 2011

Abstract

The validity of the adaptive finite element method for reconstruction of dielectrics in a symmetric structure is verified on time resolved data. Dielectric permittivity, locations and shapes/sizes of dielectric abnormalities are accurately imaged using adaptive algorithm.

1 Introduction

In this paper we formulate an adaptive algorithm using analytical developments of publications [5, 6, 8, 12, 13, 14, 15] and present numerical results for the adaptive reconstruction of the dielectric constant in a symmetric structure given backscattering data from a single measurement. Such problems arise in many real-life applications, like reconstruction of the structure of photonic crystals, and military applications such as imaging of land mines when one mine covers another. By a single measurement we understand time dependent backscattering data for a coefficient inverse problem (CIP) originating from a hyperbolic PDE, and generated either by a point source at a single location, or by a plane wave initialized in a single direction.

It is well known that the reliable numerical methods for solving CIPs faces major challenges such as nonlinearity and ill-posedness. Usually, CIPs are solved using least squares Tikhonov functionals suffering from multiple local minima or a ravine. Conventional numerical methods to solve such CIPs use different versions of Newton and gradient methods. However, these algorithms converge only if the starting point for the iterations is located in a small neighborhood of the exact solution. To solve the CIP in this paper we apply the

*Corresponding author, Department of Mathematical Sciences, Chalmers University of Technology and Gothenburg University, SE-42196 Gothenburg, Sweden, larisa@chalmers.se

†Department of Mathematical Sciences, NTNU, 7491 Trondheim, Norway, Marte.Hatlo@math.ntnu.no

‡Department of Mathematical Sciences, NTNU, 7491 Trondheim, Norway, Harald.Krogstad@math.ntnu.no

quasi-Newton method, and assume that we start our adaptive algorithm with an initial guess in a small neighborhood of the exact solution. A sufficiently good initial guess, applied in our numerical tests, is a homogeneous material. We note, that recently a new approximate globally convergent method which provides such an initial guess without any a priori knowledge of the neighborhood was developed in [10]. As soon as a first approximation to the exact solution is obtained, any locally convergent method can be applied.

The mesh-adaptive FE/FD method for solution of CIPs was first developed in [5, 6, 7, 8, 9] using a posteriori error estimate for the Lagrangian. Adaptive technique of these publications was originally applied for the solution of acoustic and elastic CIPs. The adaptivity consists of minimizing the Tikhonov functional on a sequence of locally refined meshes using the finite element discretization of the state and adjoint problems. The mesh is refined in subdomains of the computational domain, where the *a posteriori* error analysis indicates the maximal error of the computed solution.

Similarly with [5, 6, 7, 8, 9, 11] in the adaptive algorithm presented in this work we use an *a posteriori* error estimate for the Lagrangian applied to the regularized solution of the CIP. To find the error in the Lagrangian we use its Fréchet derivative. We refine the mesh in all subdomains of the computational domain where the Fréchet derivative of the Lagrangian attains its maximal values.

Similarly as for the Lagrangian, a posteriori error estimate for the Tikhonov functional was developed in recent publications [12, 13, 14]. In [12] was shown rigorously that the Fréchet derivative of the Tikhonov functional coincides with the Fréchet derivative of the Lagrangian, and in [13] was demonstrated that certain integral terms in the Fréchet derivative of the Lagrangian can be ignored. The computational tests in the present paper, as well as in previous publications, [5, 6, 7, 8, 9, 11], confirm this behavior numerically. It was shown analytically in [15] that the mesh refinement improves the accuracy of the regularized solution as long as the modulus of the gradient of the Tikhonov functional or of the Lagrangian is not too small. This was consistently observed in [5, 6, 7, 8, 9, 11, 12, 13, 14], and also in the current paper.

Our main objective has been to apply the adaptive finite element method to solve the electromagnetic CIP connected to photonic crystals, i.e. to reconstruct an unknown dielectric permittivity from backscattering data. The basic technique is to expose the structure with a known, time limited wave, and then record the backscattering waves. To solve the CIP we use the hybrid FE/FD method developed in [4]. We choose this method since it seems natural for needs of our CIP. The backscattering data of our CIP are generated by a plane wave instead of a point source, as is often the case for real-life applications. Approximating the point source with a plane wave is reasonable when we assume that the point source is far from the domain where the dielectric function should be reconstructed. Based on this setting, we split the computational domain into two domains. In the surrounding (outer) domain we initialize the plane wave and assume that the value of the dielectric function is known. A finite difference method is used in this domain. In the inner domain, where the dielectric function should be reconstructed, we apply a finite element method together with the adaptive algorithm.

The numerical tests in Section 8 have consistently demonstrated accurate reconstruction of the locations and contrasts of the dielectric permittivity in the symmetric structure from the backscattering data using the adaptive algorithm outlined in Section 7.1. In Example 2 of this Section we also show that a locally convergent quasi-Newton works well as soon good approximation to the exact solution is available. However, this method leads to a poor quality of results when the good initial guess is unavailable.

An outline of the paper is as follows. In Section 2 we formulate both forward and inverse problems. In Section 3 we present Tikhonov functional and in Section 4 - Lagrangian for our CIP. In Section 5 we formulate the finite element method and in Section 6 we present framework for the a posteriori error estimate for the Lagrangian. Further, in Section 7 we present adaptive algorithm for solution of our CIP and in Section 8 we show the results of reconstruction of dielectric function using adaptive algorithm of Section 7.

2 Forward and Inverse Problems

Our forward problem is two-dimensional, electromagnetic (EM) wave propagation in a non-magnetic, inhomogeneous and isotropic material, governed by the Cauchy problem

$$\varepsilon_r(x)u_{tt} = \Delta u, \text{ in } \mathbb{R}^2 \times (0, \infty), \tag{1}$$

$$u(x, 0) = 0, u_t(x, 0) = \delta(x - x_0). \tag{2}$$

Equation (1) may easily be derived from Maxwell equations in certain two-dimensional situations [1, 16].

In equation (1), $\varepsilon_r(x)$ is the dielectric constant, also called the relative dielectric permittivity, and defined as

$$\varepsilon_r(x) = \frac{\varepsilon(x)}{\varepsilon_0}, \tag{3}$$

where ε_0 is the dielectric permittivity of vacuum, and $\varepsilon(x)$ the dielectric permittivity of the material.

Let $c(x)$ be the speed of the EM waves in the material, and c_0 the speed of light in vacuum. Since $\varepsilon = 1/c^2$ and $\varepsilon_0 = 1/c_0^2$, the refractive index, $n(x)$, of the material is

$$n(x) = \frac{c_0}{c(x)} = \sqrt{\varepsilon_r(x)} \geq 1. \tag{4}$$

In physical experiments, the refractive index is often measured rather than the dielectric constant [14, 20].

Let $G \subset \mathbb{R}^2$ be a bounded domain with a piecewise smooth boundary, $\partial G = \Gamma_1 \cup \Gamma_2 \cup \Gamma_3$. Here, Γ_1 is the top boundary of ∂G, Γ_3 denotes the lateral boundaries, and Γ_2 the bottom boundary. Let $\Omega \subset G$ be another bounded domain with boundary $\partial\Omega = \partial\Omega_1 \cup \partial\Omega_2$, where $\partial\Omega_1$ denotes the top boundary of $\partial\Omega$, and $\partial\Omega_2$ the rest.

We shall assume that $\varepsilon_r(x)$ in equation (1) satisfies

$$\begin{aligned} &\varepsilon_r(x) \in [1,d] \ \text{ for } x \in \overline{\Omega}, \\ &\varepsilon_r(x) = 1 \text{ for } x \in G \setminus \Omega. \end{aligned} \tag{5}$$

Moreover, for the analytical derivations of minimal smoothness assumptions for state and adjoint problems of Section 3 we require

$$\varepsilon_r \in C\left(\overline{\Omega}\right) \cap H^1(\Omega), \partial_{x_i}\varepsilon_r \in L_\infty(\Omega), i = 1, 2. \tag{6}$$

We refer to [14] for these analytical derivations. However, in all computations in Section 8, the function $\varepsilon_r(x)$ is piecewise constant.

We now make some assumption about the smoothness of initial conditions (2). Since the solution of the Cauchy problem (1), (2) is not smooth, because of the $\delta-$function in the initial condition, we replace the $\delta(x - x_0)$ with its approximation $\delta_\theta(x - x_0)$. In this case smoothness would be recovered. Here $\theta \in (0,1)$ is a small number. The function $\delta_\theta(x - x_0)$ is

$$\delta_\theta(x - x_0) = \left\{ \begin{array}{c} C_\theta \exp\left(\frac{1}{|x-x_0|^2 - \theta^2}\right), \ \ |x - x_0| < \theta, \\ 0, \ \ |x - x_0| > \theta, \end{array} \right. ,$$

$$\int\limits_{\mathbb{R}^2} \delta_\theta(x - x_0)\, dx = 1.$$

Here the constant $C_\theta > 0$ is chosen to ensure the value of this integral. Since the source $x_0 \notin \overline{\Omega}$, then for sufficiently small θ

$$\delta_\theta(x - x_0) = 0 \text{ for } x \in \Omega. \tag{7}$$

Thus, the problem (1), (2) can be rewritten as

$$c(x)\, u_{tt} = \Delta u, \ \ (x,t) \in \mathbb{R}^2 \times (0, \infty), \tag{8}$$

$$u(x,0) = 0, \ u_t(x,0) = \delta_\theta(x - x_0). \tag{9}$$

Below we consider the following inverse problems:

Inverse Problem 1 (IP1). *Determine the unknown function $\varepsilon_r(x)$ for $x \in \Omega$, assuming that the following observation $u_{obs}(x,t)$ of the full solution $u(x,t)$ of (8)– (9) is known:*

$$u(x,t) = u_{obs}(x,t), \forall (x,t) \in \partial\Omega \times (0, \infty). \tag{10}$$

Inverse Problem 2 (IP2).

Determine the unknown function $\varepsilon_r(x)$ for $x \in \Omega$, assuming that the following observation $u_{obs}(x,t)$ of the full solution $u(x,t)$ of (8)– (9) is known:

$$u(x,t) = u_{obs}(x,t), \forall (x,t) \in \partial\Omega_1 \times (0, \infty), \tag{11}$$

Note that $\varepsilon_r(x) = 1$ for $x \in \mathbb{R}^2 \diagdown \Omega$.

For IP1, the function $u_{obs}(x,t)$ in (10) represents measurements in space and time of the wave field on the whole boundary $\partial\Omega$ of Ω. Thus, for IP1 we work with complete data. However, for IP2 we work with backscattering data measured only on the part $\partial\Omega_1$ of the boundary $\partial\Omega$.

Let $T > 0$ be the final observation time. Then the Cauchy problem in equation (8)–(9) with conditions (10) or (11) can be uniquely solved in $G \setminus \Omega \times (0,T)$ with the known $\varepsilon_r = 1$, see [21]. Thus, the function $u(x,t)$ is known in $G \setminus \Omega \times (0,T)$, and we can determine the following functions at the boundary $\partial\Omega$ for the case of complete data:

$$\begin{aligned} u(x,t) &= u_{obs}(x,t), \quad \forall (x,t) \in \partial\Omega \times (0,T), \\ \partial_n u(x,t) &= p(x,t), \quad \forall (x,t) \in \partial\Omega \times (0,T). \end{aligned} \tag{12}$$

In the case of backscattering data we will have functions

$$\begin{aligned} u(x,t) &= u_{obs}(x,t), \quad \forall (x,t) \in \partial\Omega_1 \times (0,T), \\ \partial_n u(x,t) &= p(x,t), \quad \forall (x,t) \in \partial\Omega_1 \times (0,T). \end{aligned} \tag{13}$$

Functions $u_{obs}(x,t)$ and $p(x,t)$ will be used in formulation of the state and adjoint problems in the next section.

3 The Tikhonov Functional

To determine $\varepsilon_r(x),\ x \in \Omega$, for IP1 we minimize the Tikhonov functional

$$J(u, \varepsilon_r) = \frac{1}{2} \int\limits_{\partial\Omega} \int\limits_0^T (u - u_{\text{obs}})^2 z_\zeta(t) \ \mathrm{d}t\mathrm{d}x + \frac{1}{2}\gamma \int\limits_{\Omega} (\varepsilon_r - \varepsilon_0)^2 \ \mathrm{d}x. \tag{14}$$

Here, the function u satisfies the state problem

$$\begin{aligned} \triangle u - \varepsilon_r u_{tt} &= 0, \quad (x,t) \in \Omega \times (0,T), \\ u(x,0) = 0,\ u_t(x,0) &= 0, \quad (x,t) \in \Omega, \\ \partial_n u &= p(x,t), \quad (x,t) \in \partial\Omega \times (0,T), \end{aligned} \tag{15}$$

where function $p(x,t)$ is defined as in (12). The observations u_{obs} are limited to a finite set of observation points at the boundary $\partial\Omega$ in IP1.

When solving IP2, u_{obs} are available only on the top boundary $\partial\Omega_1$. Thus, for the case of IP2 the Tikhonov functional will be

$$J(u, \varepsilon_r) = \frac{1}{2} \int\limits_{\partial\Omega_1} \int\limits_0^T (u - u_{\text{obs}})^2 z_\zeta(t) \ \mathrm{d}t\mathrm{d}x + \frac{1}{2}\gamma \int\limits_{\Omega} (\varepsilon_r - \varepsilon_0)^2 \ \mathrm{d}x, \tag{16}$$

and the function u here satisfies the following state problem

$$\begin{aligned}\triangle u - \varepsilon_r u_{tt} &= 0, \quad (x,t) \in \Omega \times (0,T),\\ u(x,0) = 0,\ u_t(x,0) &= 0, \quad (x,t) \in \Omega,\\ \partial_n u &= p(x,t), \quad (x,t) \in \partial\Omega_1 \times (0,T).\end{aligned} \tag{17}$$

with function $p(x,t)$ given in (13).

The function $z_\zeta(t) \in C^\infty[0,T]$ in (14) ensures that the compatibility conditions are satisfied for the adjoint problem (18) at $t = T$, and is defined as

$$z_\zeta(t) = \begin{cases} 1 \text{ for} \in [0, T-\zeta], \\ 0 \text{ for } t \in \left(T - \frac{\zeta}{2}, T\right], \\ z_\zeta(t) \in (0,1) \quad \text{for } t \in \left(T-\zeta, T-\frac{\zeta}{2}\right). \end{cases}$$

For the second part of the Tikhonov functional (14) or (16), γ is a small regularization parameter, and ε_0 is the initial guess for ε_r. The $L_2(\Omega)$ norm is used in the regularization term because we work with a finite dimensional space of finite elements in the numerical examples of Section 8.

The adjoint problem for both IP1 and IP2 for the function $\lambda(x,t)$ is

$$\begin{aligned}\varepsilon_r \lambda_{tt} - \Delta\lambda &= 0, \quad (x,t) \in \Omega \times (0,T),\\ \partial_n \lambda &= (u_{obs} - u) z_\zeta(t) \text{ on } \Omega \times (0,T),\\ \lambda(x,T) = \lambda_t(x,T) &= 0, \quad x \in \Omega.\end{aligned} \tag{18}$$

This problem is solved backwards in time. Here, function $u(x,t)$ is the solution of the state problem (15) for IP1 and (17) for IP2, and the function $u_{obs}(x,t)$ is defined by (12) for IP1 and by (13) for IP2, correspondingly.

4 The Lagrangian and its Fréchet Derivative

In order to minimize the Tikhonov functional (14) for IP1 or (16) for IP2, we introduce the associated Lagrangian and derive its Fréchet derivative by a heuristic approach. Below we will derive the Fréchet derivative of the Lagrangian for IP1, since the Fréchet derivative of the Lagrangian for IP2 can be derived similarly. In this derivation we assume that the functions u, λ, and ε_r can be varied independently. However, when the Fréchet derivative is calculated, we assume that the solutions of the forward and adjoint problems depend on ε_r. A rigorous derivation of the Fréchet derivative can be found in [15] and is far from trivial since it requires some smoothness assumptions for the solutions of the state and adjoint problems.

Let us introduce the following spaces,

$$\begin{aligned}
H_u^2(\Omega \times (0,T)) &= \{f \in H^2(\Omega \times (0,T)) : f(x,0) = f_t(x,0) = 0\}, \\
H_u^1(\Omega \times (0,T)) &= \{f \in H^1(\Omega \times (0,T)) : f(x,0) = 0\}, \\
H_\lambda^2(\Omega \times (0,T)) &= \{f \in H^2(\Omega \times (0,T)) : f(x,T) = f_t(x,T) = 0\}, \\
H_\lambda^1(\Omega \times (0,T)) &= \{f \in H^1(\Omega \times (0,T)) : f(x,T) = 0\}, \\
U &= H_u^2(\Omega \times (0,T)) \times H_\lambda^2(\Omega \times (0,T)) \times C^2(\bar{\Omega}), \\
\bar{U} &= H_u^1(\Omega \times (0,T)) \times H_\lambda^1(\Omega \times (0,T)) \times L_2(\Omega),
\end{aligned} \tag{19}$$

where all functions are real valued. Hence, U is included and dense in $\bar{U}$. In order to incorporate the constraint imposed by equation (1), we introduce the Lagrangian

$$L(v) = J(u, \varepsilon_r) + \int_0^T \int_\Omega \lambda\left(\varepsilon_r u_{tt} - \Delta u\right) \mathrm{d}x\mathrm{d}t, \tag{20}$$

where λ is the Lagrange multiplier and $v = (u, \lambda, \varepsilon_r) \in U$. Clearly, if u is a solution of equation (1), then $L(v) = J(u, \varepsilon_r)$. Integrating by parts in equation (20) leads to

$$L(v) = J(u, \varepsilon_r) - \int_0^T \int_\Omega \varepsilon_r u_t \lambda_t \mathrm{d}x\mathrm{d}t + \int_0^T \int_\Omega \nabla u \nabla \lambda \mathrm{d}x\mathrm{d}t - \int_0^T \int_{\partial\Omega} p\lambda \mathrm{d}\sigma\mathrm{d}t. \tag{21}$$

A stationary point of the functional $L(v)$, satisfies

$$L'(v)(\bar{v}) = 0, \quad \forall \bar{v} = (\bar{u}, \bar{\lambda}, \bar{\varepsilon_r}) \in \bar{U}, \tag{22}$$

where $L'(v)$ is the Fréchet derivative of the Lagrangian L at v. In order to find the gradient, one considers $L\left(v + \bar{v}\right) - L\left(v\right), \ \forall \bar{v} \in \bar{U}$, and single out the linear part of this expression with respect to $\bar{v}$. Hence, from equations (21) and (22) we obtain

$$\begin{aligned}
L'(v)(\bar{v}) = &\int_0^T \int_\Omega \bar{u}(u - u_{\mathrm{obs}}) z_\zeta\left(t\right) \mathrm{d}x\mathrm{d}t + \gamma \int_\Omega \bar{\varepsilon_r}(\varepsilon_r - \varepsilon_0)\mathrm{d}x \\
&- \int_0^T \int_\Omega \varepsilon_r (u_t \bar{\lambda}_t + \bar{u}_t \lambda_t) \mathrm{d}x\mathrm{d}t - \int_0^T \int_\Omega \bar{\varepsilon_r} u_t \lambda_t \mathrm{d}x\mathrm{d}t \\
&+ \int_0^T \int_\Omega (\nabla u \nabla \bar{\lambda} + \nabla \bar{u} \nabla \lambda) \mathrm{d}x\mathrm{d}t - \int_0^T \int_{\partial\Omega} p\bar{\lambda} \mathrm{d}\sigma\mathrm{d}t.
\end{aligned} \tag{23}$$

Integration by parts now brings out $\bar{v}$:

$$\begin{aligned} L'(v)(\bar{v}) = & \int_0^T \int_\Omega \bar{\lambda}(\varepsilon_r u_{tt} - \Delta u)\mathrm{d}x\mathrm{d}t - \int_0^T \int_{\partial\Omega} p\bar{\lambda}\mathrm{d}\sigma\mathrm{d}t \\ & + \int_0^T \int_{\partial\Omega} \bar{u}(u - u_{\mathrm{obs}})z_\zeta(t) + \int_0^T \int_\Omega \bar{u}(\varepsilon_r \lambda_{tt} - \Delta\lambda)\mathrm{d}x\mathrm{d}t \\ & + \int_\Omega \bar{\varepsilon_r} \left[\gamma(\varepsilon_r - \varepsilon_0) - \int_0^T u_t\lambda_t \mathrm{d}t \right] \mathrm{d}x. \end{aligned} \tag{24}$$

Hence, equations (22) and (23) imply that every integral term in equation (24) equals zero. Thus, if $(u, \lambda, \varepsilon_r) = v \in U$ is a minimizer of the Lagrangian $L(v)$ in equation (21), then the terms containing $\bar{\lambda}$ correspond to the forward (or state) problem (15). Furthermore, the terms with $\bar{u}$ are the weak form of the adjoint state equation (18).

We can find $\varepsilon_r(x)$ from the equation

$$\varepsilon_r(x) = \frac{1}{\gamma} \int_0^T u_t\lambda_t \mathrm{d}t + \varepsilon_0, \quad x \in \Omega.$$

To do this, we need to solve the equation above with respect to the function ε_r, where the functions $u \in H_u^1$ and $\lambda \in H_\lambda^1$ are weak solutions of the problems (15) and (18), respectively.

The boundary value adjoint problem (18) is solved backwards in time. Uniqueness and existence theorems for the initial/boundary value problems, equations (15) and (18), including weak solutions, can be found in Chapter 4 of [21]. The Lagrangian $L(v)$ is minimized iteratively by obtaining weak solutions of the boundary value problems (15) and (18) on each step by means of a FEM formulation.

5 A Finite Element Method to solve equation (22)

For discretization of (21) we use the finite element method. Let us introduce the finite element spaces $W_h^u \subset H_u^1(\Omega \times (0,T))$ and $W_h^\lambda \subset H_\lambda^1(\Omega \times (0,T))$ for u and λ, respectively. These spaces consist of continuous piecewise linear functions in space and time, satisfying the initial conditions $u(x,0) = 0$ for $u \in W_h^u$, and $\lambda(x,T) = 0$ for $\lambda \in W_h^\lambda$. We also introduce the finite element space $V_h \subset L_2(\Omega)$ consisting of piecewise constant functions for the coefficient $\varepsilon_r(x)$ and denote $W_h^u \times W_h^\lambda \times V_h$ by U_h, $U_h \subset \bar{U}$. Thus, U_h is a discrete analogue of $\bar{U}$.

The FEM for (22) now consists of finding $v_h \in U_h$, so that

$$L'(v_h; \bar{v}) = 0, \quad \forall \bar{v} \in U_h. \tag{25}$$

6 An a Posteriori Error Estimate for the Lagrangian

We shall now present the main steps in the derivation of an *a posteriori* bound for the error of the finite element approximation to the function ε_r.

Let $v \in U$ be a minimizer of the Lagrangian L on the space $\bar{U}$, and v_h a minimizer of this functional on U_h. That is, v is a solution of (22) and v_h is a solution of (25).

Since adaptivity is a locally convergent numerical method, we may assume that we work in a small neighborhood of the exact solution $v^* \in U$ of the full problem. This means that if ${\varepsilon_r}^*$ is the exact solution of IP1 or IP2, then $u^* = u(\varepsilon_r^*)$ is the exact solution of (15), and $u^* - u^*_{obs} = 0$. Moreover, the solution of the adjoint problem (18) is $\lambda(\varepsilon_r^*) = 0$. However, we can never get exact measurements u^*_{obs} since they always suffer from a certain noise level. Thus, we assume that

$$\|v - v^*\|_{\bar{U}} \leq \sigma, \tag{26}$$

where σ is sufficiently small. Here, $v = (u(\varepsilon_r), \lambda(\varepsilon_r), \varepsilon_r)$, and we call ε_r the regularized solution of the minimization problem (14). Below we present the error in the Lagrangian for the regularized coefficient ε_r, see also the discussion in Introduction.

The *a posteriori* error estimate $L(v) - L(v_h)$ for the Lagrangian is based on the

$$\begin{aligned} L(v) - L(v_h) &= \int_0^1 \frac{\mathrm{d}}{\mathrm{d}s} L(sv + (1-s)v_h) \mathrm{d}s \\ &= \int_0^1 L'(sv + (1-s)v_h)\,(v - v_h)\,\mathrm{d}s = L'(v_h)\,(v - v_h) + R, \end{aligned} \tag{27}$$

where $R = \mathcal{O}(\sigma^2)$. Since σ is small, we may ignore R in (27), see details in [15] and [3] for similar results in the case of a general nonlinear operator equation.

Using Galerkin orthogonality (25) along with the splitting $v - v_h = (v - v_h^I) + (v_h^I - v_h)$, where v_h^I is an interpolant of v, we obtain the error representation

$$L(v) - L(v_h) \approx L'(v_h)\,(v - v_h^I), \tag{28}$$

expressing the residual in terms of the interpolation error. The splitting is one of the key elements in the adaptivity technique, because it allows us to use Galerkin orthogonality (25) and standard estimates for interpolation errors. We estimate $v - v_h^I$ in terms of derivatives of v, the mesh parameter h in space and τ in time. Finally, we approximate the derivatives of v by the corresponding derivatives of v_h, see [5, 9]. Numerical experiments in previous publications [5, 8, 9, 11, 15] and of this paper show that the dominating contribution to the error in the Lagrangian occurs in the residuals of the reconstruction of ε_r, which may be estimated from the above by

$$\gamma \max_{\overline{\Omega}} |\varepsilon_{rh} - \varepsilon_0| + \max_{\overline{\Omega}} \int_0^T |u_{ht}\lambda_{ht}|\,\mathrm{d}t. \tag{29}$$

While the integral terms in the *a posteriori* error for the Lagrangian was ignored due to numerical observations in the publications cited above, this fact was analytically explained in [13]. Thus, the error in the Lagrangian may be decreased by refining the grid locally in the regions where the absolute value of the gradient with respect to ε_r attains its maximum.

7 The Adaptive Algorithm

We minimize the Tikhonov functional using the quasi-Newton method with the classical BFGS update formula, [22]. We denote the nodal values of the gradient function $g^m(x)$ as

$$g^m(x) = \gamma({\varepsilon_r}_h^m - \varepsilon_0) - \int_0^T u_{ht}^m \lambda_{ht}^m \,\mathrm{d}t. \tag{30}$$

The FEM solutions $u_h^m \in W_h^u$ and $\lambda_h^m \in W_h^\lambda$ are obtained by solving the boundary value problems (1) and (18) with $\varepsilon_r := {\varepsilon_r}_h^m$.

Then we can compute a sequence $\{{\varepsilon_r}_h^m\}_{m=1,...,M} \subset V_h$ of approximations to ε_r defined by the iteration

$${\varepsilon_r}_h^{m+1}(x) = {\varepsilon_r}_h^m(x) - \alpha H^m g^m(x),\ m = 1, ..., M. \tag{31}$$

Here α is the step length in the gradient method, computed by the line-search algorithm, $g^m(x)$ is the gradient, and H^m an approximation to the inverse of the Hessian of the Lagrangian L, updated by the BFGS formula [22].

7.1 The Algorithm

Step 0. Choose an initial mesh K_h in the domain Ω and a time partition J_τ of the time interval $(0, T)$. Start with the initial approximation ${\varepsilon_r}_h^0 := \varepsilon_0$ and compute the sequence of functions ${\varepsilon_r}_h^m$ in the steps described below.

Step 1. Compute FEM solutions $u_h\left(x, t, {\varepsilon_r}_h^m\right), \lambda_h\left(x, t, {\varepsilon_r}_h^m\right)$ of the state and adjoint problems (15), (18) on K_h, J_τ.

Step 2. Update the coefficient $\varepsilon_r := {\varepsilon_r}_h^{m+1}$ on K_h using (31).

Step 3. Stop computing the functions ${\varepsilon_r}_h^m$ if either $||g^m||_{L_2(\Omega)} \leq \theta$, or the norms $||g^m||_{L_2(\Omega)}$ abruptly grow, or the norms $||g^m||_{L_2(\Omega)}$ are stabilized, where $0 < \theta < 1$ is chosen by the user. Otherwise, set $m := m + 1$ and go to Step 1.

Step 4. Compute the function $A(x) = \left|g_h^m\left(x\right)\right|$. Refine the mesh where

$$A(x) \geq \beta \max_{\overline{\Omega}} A(x). \tag{32}$$

Here, the tolerance number β is chosen by the user.

Step 5. Construct a new mesh K_h and a new time partition J_τ of the time interval $(0, T)$. The new time step τ of J_τ should satisfy the CFL condition (35). Interpolate the initial approximation ${\varepsilon_r}_h^0$ on the new mesh. Return to Step 1 and perform all the steps above on the new mesh.

Step 6. Stop the mesh refinements when the stopping criterion described in Step 3 is satisfied.

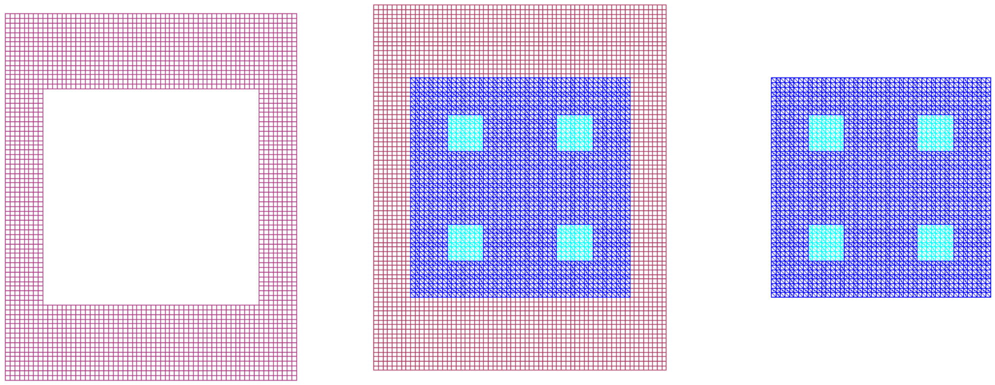

Figure 1: The hybrid mesh (b) is a combination of a structured mesh (a), where FDM is applied, and a mesh (c), where we use FEM, with a thin overlapping layer of structured elements.

8 Numerical Examples

In this section we present results of numerical studies of the adaptive algorithm of Section 7.1. To solve the forward and adjoint problems, we use the hybrid FE/FD method described in [4]. The adaptive algorithm is tested on the reconstruction of the periodic structure given in Figure 1-c).

The computational domain is defined as $G = [-4.0, 4.0] \times [-5.0, 5.0]$. Next, G is split into a finite element domain $\Omega = \Omega_{FEM} = [-3.0, 3.0] \times [-3.0, 3.0]$ with an unstructured mesh, and a surrounding domain Ω_{FDM} with a structured mesh, see Figure 1. Between Ω_{FEM} and Ω_{FDM} there is an overlapping layer consisting of structured elements. The space mesh consists of triangles in Ω_{FEM}, and squares in Ω_{FDM}, with mesh size $\tilde{h} = 0.125$ in the overlapping region. At the top and bottom boundaries of G we use first-order absorbing boundary conditions [18]. At the lateral boundaries, Neumann boundary conditions allow us to assume an infinite space-periodic structure in the lateral direction.

The forward problem in all our tests is

$$
\begin{aligned}
\Delta u - \varepsilon_r(x) \frac{\partial^2 u}{\partial t^2} &= 0, \quad (x,t) \in \Omega \times (0,T), \\
u(x,0) &= 0, \frac{\partial u}{\partial t}(x,0) = 0, \quad x \in \Omega, \\
\partial_n u\big|_{\Gamma_1} &= f(t), \text{ on } \Gamma_1 \times (0, T_1], \\
\partial_n u\big|_{\Gamma_1} &= -u_t, \text{ on } \Gamma_1 \times (T_1, T), \\
\partial_n u\big|_{\Gamma_2} &= -u_t, \text{ on } \Gamma_2 \times (0, T), \\
\partial_n u\big|_{\Gamma_3} &= 0, \text{ on } \Gamma_3 \times (0, T).
\end{aligned}
\tag{33}
$$

To generate data at the observation points, we solve the forward problem (33) in the domain Ω with a plane wave pulse given as

$$\partial_n u\big|_{\Gamma_1} = ((\sin(\omega t - \pi/2) + 1)/10),\ 0 \leq \frac{2\pi}{\omega} = T_1. \tag{34}$$

The wave field thus initiates at the boundary Γ_1, which in our examples represents the top boundary of the computational domain G, and propagates in normal direction n into G with $\omega = 6$.

In the various examples of this section, the observation points are placed either on the upper boundary of Ω_{FEM} (Test 1 of Section 8.1.1, or on both the lower and top boundaries of Ω_{FEM} (Test 2 of Section 8.1 and Example 2 of Section 8.2).

To generate data for the inverse problem, we solve the forward problem (33) with $T = 12$, with the value of the dielectric constant $\varepsilon_r = 4$ inside the four small squares in Figure 1-c), and with $\varepsilon_r = 1.0$ everywhere else. Our goal is to reconstruct the electric permittivity ε_r in Ω_{FEM}. We enforce $\varepsilon_r(x)$ to belong to the set of admissible coefficients, $C_M = \{\varepsilon_r \in C(\Omega) | 1.0 < \varepsilon_r(x) < 4.0\}$ as follows: if $0 < \varepsilon_r(x_0) < 1.0$ for some point $x_0 \in \Omega$ then we set $\varepsilon_r(x_0) = 1.0$.

Since an explicit scheme [5, 9] is used to solve the forward and adjoint problems, we choose a time step τ according to the Courant-Friedrichs-Levy (CFL) stability condition in two dimensions, see, for example, [17]

$$\tau \leq \frac{h}{\sqrt{2}\varepsilon_{r\max}}. \tag{35}$$

The CFL condition assures a stable time discretization. Here, h is the minimal local mesh size, and $\varepsilon_{r\max}$ an *a priori* upper bound for the coefficient computed on the mesh K_h.

In some of the tests we have added relative random noise in the observations. Noisy data, u_σ, are defined by

$$u_\sigma = u_{\text{obs}} + \alpha_2(u_{\max} - u_{\min})\frac{\sigma}{100}, \tag{36}$$

where α_2 is a random number in the interval $[-1; 1]$, $u_{\max}$ and $u_{\min}$ are the maximal and minimal values of the computed observations u_{obs}, correspondingly, and σ is the noise expressed in percents. In all tests, we have applied some smoothing in the update of the coefficient by locally averaging over neighboring elements. We choose computationally the value of the tolerance β in (32) in all examples. Usually, this value is $\beta = 0.7$, but can vary as $0.1 \leq \beta \leq 0.7$ from the coarse to more refined mesh.

8.1 Example 1

In Test 1 and Test 2 the initial guess is chosen as $\varepsilon_{r0} = 1.0$ at all points in the computational domain Ω_{FEM}. In Test 1, the observation points are all placed only at the top boundary of Ω_{FEM}, and thus we work with backscattering data, while in Test 2 we have observation points on both the upper and lower boundary of Ω_{FEM}. The computations have been performed for different regularization parameters γ and with different noise level σ in (36) added to the data.

8.1.1 Test 1: Backscattering Data

In Test 1 we solve IP2 and minimize the Tikhonov functional (16) using the adaptive algorithm of Section 7.1. The observation points are placed at $\partial\Omega_1$, the top of Ω_{FEM}. When solving IP2 we use following conditions

$$\begin{aligned} u\left(x,t\right) &= u_{obs}\left(x,t\right), \forall \left(x,t\right) \in \partial\Omega_1 \times \left(0,T\right), \\ u(x,t) &= 0, \forall \left(x,t\right) \in \partial\Omega_2 \times \left(0,T\right). \end{aligned} \tag{37}$$

Second condition in (37) follows from the computational simulations of the forward problem (33) when we observed that values of function $u(x,t)$ at $\partial\Omega_1 \times (0,T)$ are much larger then values of function $u(x,t)$ at $\partial\Omega_2 \times (0,T)$.

Let us denote $S_1 = \partial\Omega_1 \times (0,T)$. To check convergence of the adaptive algorithm of Section 7.1, for every refined mesh we calculate the L_2-norms $||u_h - u_{\text{obs}}||_{L_2(S_1)}$. Table 1 shows a comparison of the norms for different regularization parameters. The L_2-norms $||u_h - u_{\text{obs}}||_{L_2(S_1)}$ in Table 1 are given only for the fourth refined mesh and as long as they are decreasing. The noise level in these computations is $\sigma = 0\%$. From Table 1 we observe the smallest value of $||u_h - u_{\text{obs}}||_{L_2(S_1)}$ is obtained with a regularization parameter $\gamma = 0.01$. The results with $\gamma = 0.1$ are less accurate, indicating this value is too large and involve too much regularization. We may also note that the norm is reduced by approximately a factor of five between the first and last optimization iteration.

	$\gamma = 10^{-1}$	$\gamma = 10^{-2}$	$\gamma = 10^{-3}$	$\gamma = 10^{-4}$
it = 1	0.103	0.104	0.104	0.104
it = 2	0.0714	0.0714	0.0354	0.0714
it = 3	0.0620	0.0614	0.0714	0.0702
it = 4		0.0344	0.0694	0.0463
it = 5		0.0230	0.0451	0.0291
it = 6			0.0282	0.0255
it = 7			0.0246	

Table 1: Example 1, Test 1. Computed norms $||u_h - u_{\text{obs}}||_{L_2(S_1)}$ on the fourth refined mesh for different values of the regularization parameter γ.

In Figures 2-e), f), g), h) we show the reconstructed coefficient ε_r on the first, second, third and fourth adaptively refined meshes. Corresponding adaptively refined meshes are presented in Figures 2-a), b), c), d). These computations were done with noise level $\sigma = 0\%$ and regularization parameter $\gamma = 0.01$. Our final solution corresponds to the fourth refined mesh and is presented in Figure 2-h). One can see from this Figure that we are able quite accurately reconstruct from the backscattering data the symmetric location of the four small squares given in Figure 1-c). We obtain inclusions/background contrast 2.76 : 1 on the fourth refined mesh compared with 1.88 : 1 on the first refined mesh. The value of $\epsilon_r = 1$ outside of inclusions is also imaged accurately. Thus, on the fourth refined mesh we have reconstructed 69% of the real contrast in inclusions. We recall that this exact contrast was 4. Our results clearly indicate that contrasts and locations of inclusions are improved as the mesh is refined.

Next, the performance of the adaptive algorithm of Section 7.1 was tested on noisy data with a fixed $\gamma = 0.01$. Noise was added to the data as described in equation (36). The computed norms $||u_h - u_{\text{obs}}||_{L_2(S_1)}$ on the fourth adaptively refined mesh are given for different noise levels in Table 2. These norms are shown as long as they decrease. From results of Table 2 we conclude that our algorithm is stable when computing it with small values of the noise $\sigma = 0, 1, 3, 5\%$, and the algorithm deteriorates when adding more than 5% noise to the data.

	$\sigma = 0$	$\sigma = 1.0$	$\sigma = 3.0$	$\sigma = 5.0$	$\sigma = 7.0$	$\sigma = 10.0$
it = 1	0.104	0.109	0.125	0.150	0.180	0.230
it = 2	0.0714	0.0830	0.114	0.148	0.184	0.239
it = 3	0.0614	0.0635	0.0801	0.109	0.147	0.211
it = 4	0.0344	0.0349	0.0610	0.0972	0.137	0.209
it = 5	0.0230	0.0282	0.0599	0.0971		0.204
it = 6		0.0280	0.0597			0.204
it = 7						0.202
it = 8						0.202
it = 9						0.200
it = 10						0.200
it = 11						0.199

Table 2: Example 1, Test 1. Computed norms $||u_h - u_{\text{obs}}||_{L_2(S_1)}$ on the fourth refined mesh for $\gamma = 0.01$ and different noise level σ.

8.1.2 Test 2

Let now decompose the boundary $\partial\Omega$ of the domain Ω into three parts such that $\partial\Omega = \partial\Omega_1 \cup \partial\Omega_2 \cup \partial\Omega_3$, where $\partial\Omega_1$ is the top boundary of $\partial\Omega$, $\partial\Omega_3$ denotes the lateral boundaries, and $\partial\Omega_2$ the bottom boundary. Computations in this test are performed when data at the observation points u_{obs} are saved both on the upper $\partial\Omega_1$ and lower $\partial\Omega_2$ boundaries of Ω_{FEM}. More precisely, to generate data for the inverse problem we solve the forward problem (33) in time $[0, T]$ with $T = 12$ and register values of the function $u(x, t)$ on $\partial\Omega_1$ and $\partial\Omega_2$ such that when solving our CIP we use following conditions

$$\begin{aligned} u\left(x,t\right) &= u_{obs}\left(x,t\right), \forall\left(x,t\right) \in \partial\Omega_1 \cup \partial\Omega_2 \times \left(0,T\right), \\ u(x,t) &= 0, \forall\left(x,t\right) \in \partial\Omega_3 \times \left(0,T\right). \end{aligned} \tag{38}$$

Again, second condition in (38) follows from the computational simulations of the forward problem (33) when we observed that values of function $u(x, t)$ at $\partial\Omega_1 \cup \partial\Omega_2 \times (0, T)$ are

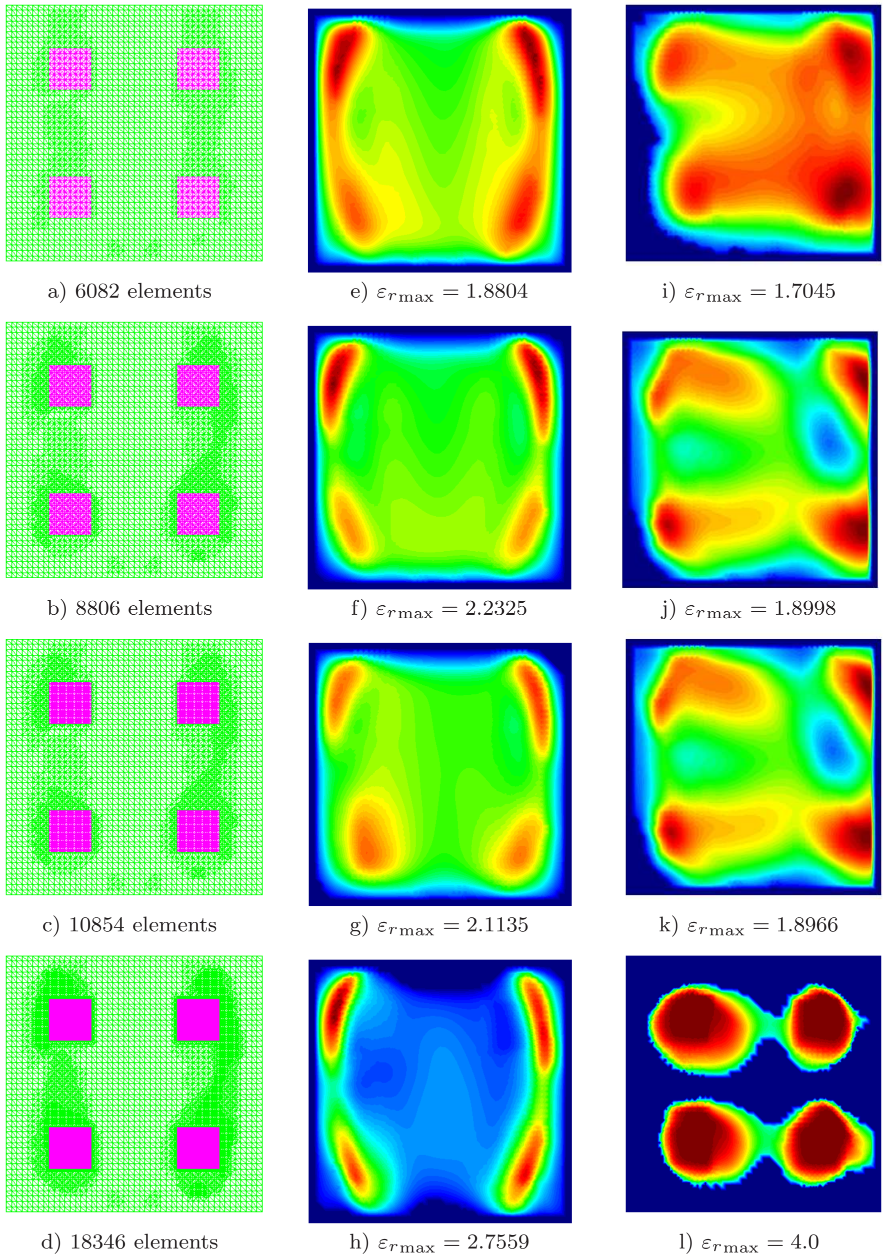

Figure 2: Example 1. a), b), c), d) The adaptively refined meshes in Test 1. e), f), g), h) The reconstructed coefficient $\varepsilon_r(x)$ in Test 1. i), j), k), l) The reconstructed coefficient $\varepsilon_r(x)$ in Test 2. Here, red color corresponds to the maximal value of ε_r on the corresponding meshes, and blue color to the minimal, $\varepsilon_{r\min} = 1.0$ in all plots. The results of reconstruction in Test 2 are better the the results of Test 1 because we have twice as much information in Test 2.

much larger then values of function $u(x,t)$ at $\partial\Omega_3 \times (0,T)$. Thus, we have twice as much information then in Test 1 and therefore expect to get a quantitative better reconstruction of the structure.

Figures 2-i), j), k), l) show the reconstructed coefficient $\varepsilon_r(x)$ when the noise level in the data was $\sigma = 1\%$ and the regularization parameter $\gamma = 0.01$. On these Figures the reconstructed coefficient ϵ_r is presented on the first, second, third and fourth adaptively refined meshes at the final optimization iteration. The final solution corresponds to the fourth refined mesh and is presented in Figure 2-l). One can see from this Figure that we are able very accurately reconstruct the symmetric location of the four small squares given in Figure 1-c). We obtain inclusions/background contrast $4.0 : 1$ on the fourth refined mesh compared with $1.7 : 1$ on the first refined mesh. The value of $\epsilon_r = 1$ outside of inclusions is also imaged accurately. Thus, on the fourth refined mesh we have reconstructed 100% of the real contrast in inclusions. This example demonstrates that observation data collected both on the top and bottom boundaries allows to get excellent reconstruction results compared with backscattering data only. However, the case of the backscattering data is realistic one.

Let us denote $S_2 = \partial\Omega_1 \cup \partial\Omega_2 \times (0,T)$. In Figures 3 and 4 we present a comparison of the computed L_2-norms $||u_h - u_{\text{obs}}||_{L_2(S_2)}$ depending on the relative noise σ on the different meshes. The norms are plotted as long as they decrease. From these results we conclude that the reconstruction is stable on the two, three and four times refined meshes, even when $\sigma = 10\%$ relative noise has been added to the data. Recall that in Test 1 we observed stability only up to 5% error in the data.

In Figure 5 we show a comparison of the computed L_2-norms $||u_h - u_{\text{obs}}||_{L_2(S_2)}$ depending on the different regularization parameters γ. We see that the smallest value of $||u_h - u_{\text{obs}}||_{L_2(S_2)}$ is obtained with regularization parameter $\gamma = 0.01$, while $\gamma = 0.1$ is again too large and involve too much regularization. Figure 6-b) shows that the best results are obtained on the finest mesh with 18346 elements, where $||u_h - u_{\text{obs}}||_{L_2(S_2)}$ is reduced by approximately a factor of 7 between the first and the last optimization iterations. On the same Figure we observe that norm $||u_h - u_{\text{obs}}||_{L_2(S_2)}$ is reduced by approximately a factor of 3.5 between the first and the last optimization iterations on a coarse mesh with 6082 elements.

8.2 Example 2

The goal of this test is to show that the quasi-Newton method can deteriorate if a good first initial guess of the function ϵ_r is unavailable. To generate data at the observation points for the inverse problem, we solve the forward problem (33) for the same structure as in Figure 1. As before, we assume that $\varepsilon_r = 1$ in Ω_{FDM}. The trace of the incoming wave is measured on both the lower and the upper boundaries of the computational domain Ω_{FEM} as in Example 1, Test 2. Now we choose the initial guess for the function ε_r as $\varepsilon_{r0} = 1.5$ at the inner points of the computational domain Ω_{FEM}. The parameter $\varepsilon_r(x)$ is enforced to belong to the set of the admissible parameters C_M as defined above. The computations in the quasi-Newton procedure are stopped when the norms $||u_h - u_{\text{obs}}||_{L_2(S_2)}$ are stabilized.

We use the same adaptive algorithm of Section 7.1 as in the Example 1. In Figure 7-f), g),

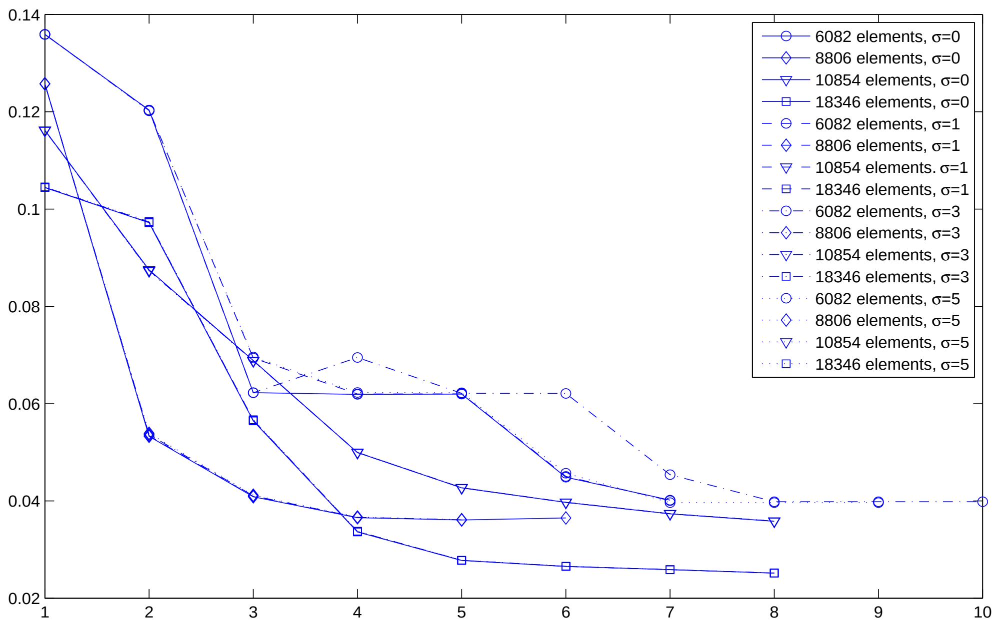

Figure 3: Example 1, Test 2: $||u_h - u_{\text{obs}}||_{L_2(S_2)}$ on the first, second, third and fourth adaptively refined meshes. The computations were performed with noise level $\sigma = 0, 1, 3\%$ and $\sigma = 5\%$ and with the regularization parameter $\gamma = 0.01$. Here, the x-axis denotes the number of optimization iterations.

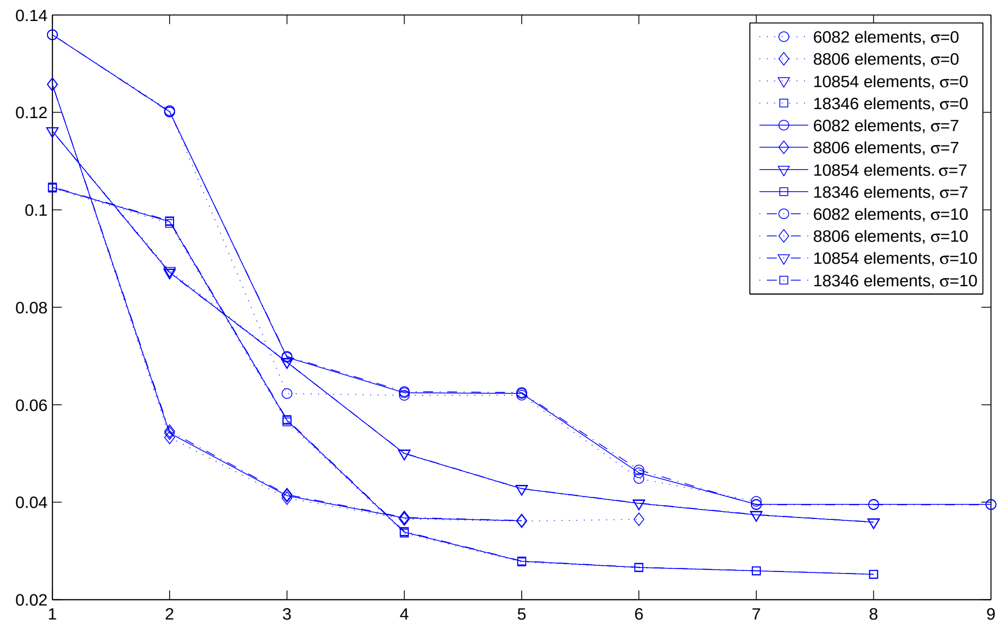

Figure 4: Example 1, Test 2: $||u_h - u_{\text{obs}}||_{L_2(S_2)}$ on the first, second, third and fourth adaptively refined meshes. The computations were performed with noise level $\sigma = 0, 7\%$ and 10% and with the regularization parameter $\gamma = 0.01$. Here, the x-axis denotes the number of optimization iterations.

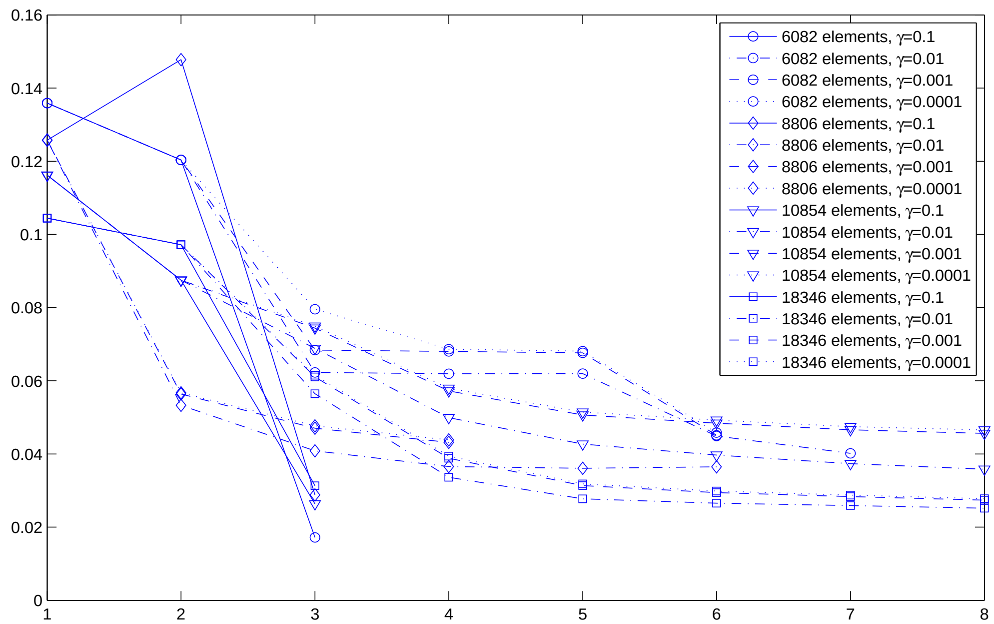

Figure 5: Example 1, Test 2: $||u_h - u_{\text{obs}}||_{L_2(S_2)}$ on the first, second, third and fourth adaptively refined meshes. The noise level in data is $\sigma = 1\%$ and the regularization parameter $\gamma = 0.1, 0.01, 0.001$ and $\gamma = 0.0001$. Here, the x-axis denotes the number of optimization iterations.

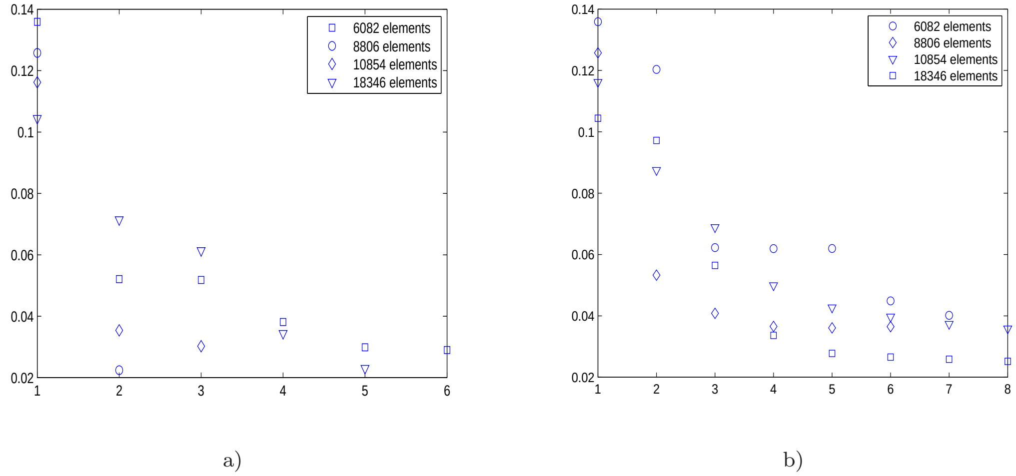

Figure 6: Example 1: computed L_2 norms on the first, second, third and firth adaptively refined meshes. In a) we show computed norms $||u_h - u_{\text{obs}}||_{L_2(S_1)}$ when noise level $\sigma = 0\%$ and the regularization parameter $\gamma = 0.01$ in Test 1, and in b) norms $||u_h - u_{\text{obs}}||_{L_2(S_2)}$ are presented when noise level $\sigma = 1\%$ and the regularization parameter $\gamma = 0.01$ in Test 2. Here, the x-axis denotes the number of optimization iterations.

h), i), j) we present the results of the reconstruction of the function ϵ_r when the noise level in the data is $\sigma = 0\%$, and in Figure 7-k), l), m), n), o) the noise level is $\sigma = 5\%$. As before, the noise is computed using (36). For both noise levels we obtain excellent inclusions/background contrast 3.99 : 1 on the fourth refined mesh. The value of $\epsilon_r = 1$ outside of inclusions is also imaged accurately. Figure 7 shows that the reconstruction of the function ϵ_r is improved as the meshes are refined. However, the locations of the imaged right squares are shifted slightly to the right because of the smoothing procedure over the neighboring elements. Note that the coarse and the ones refined meshes are the same as in the Example 1, Test 2, while the two, three and fourth refined meshes are different.

On Figures 8 and 9 we show the one-dimensional cross-sections of the image of the functions ${\varepsilon_r}_h^m$ along the vertical line passing through the middle of the left small square, with the correct $\varepsilon_r(x)$ superimposed. In Figure 8 the noise level in data is $\sigma = 0\%$ and in Figure 9 it is $\sigma = 5\%$. Using these Figures we observe that the images deteriorate or achieve a local minima on the coarse mesh. The reconstruction is dramatically improved as the meshes are refined using the adaptive algorithm of Section 7.1.

We also performed similar reconstruction tests with another initial guess $\varepsilon_{r0} = 2.0$ at the inner points of Ω_{FEM}. The reconstructed function ϵ_r (not shown here) is deteriorated not only on the coarse mesh, but also on the one and two times refined meshes. Our tests allow conclude that the adaptivity works in a neighborhood of an initial guess $1 \leq \varepsilon_{r0} \leq 1.5$. We note that the usual quasi-Newton algorithm without adaptivity works well with the guess $\varepsilon_{r0} = 1$ and deteriorates for $\varepsilon_{r0} = 1.5$, see Figure 7-f), k) and Test 5 in [10].

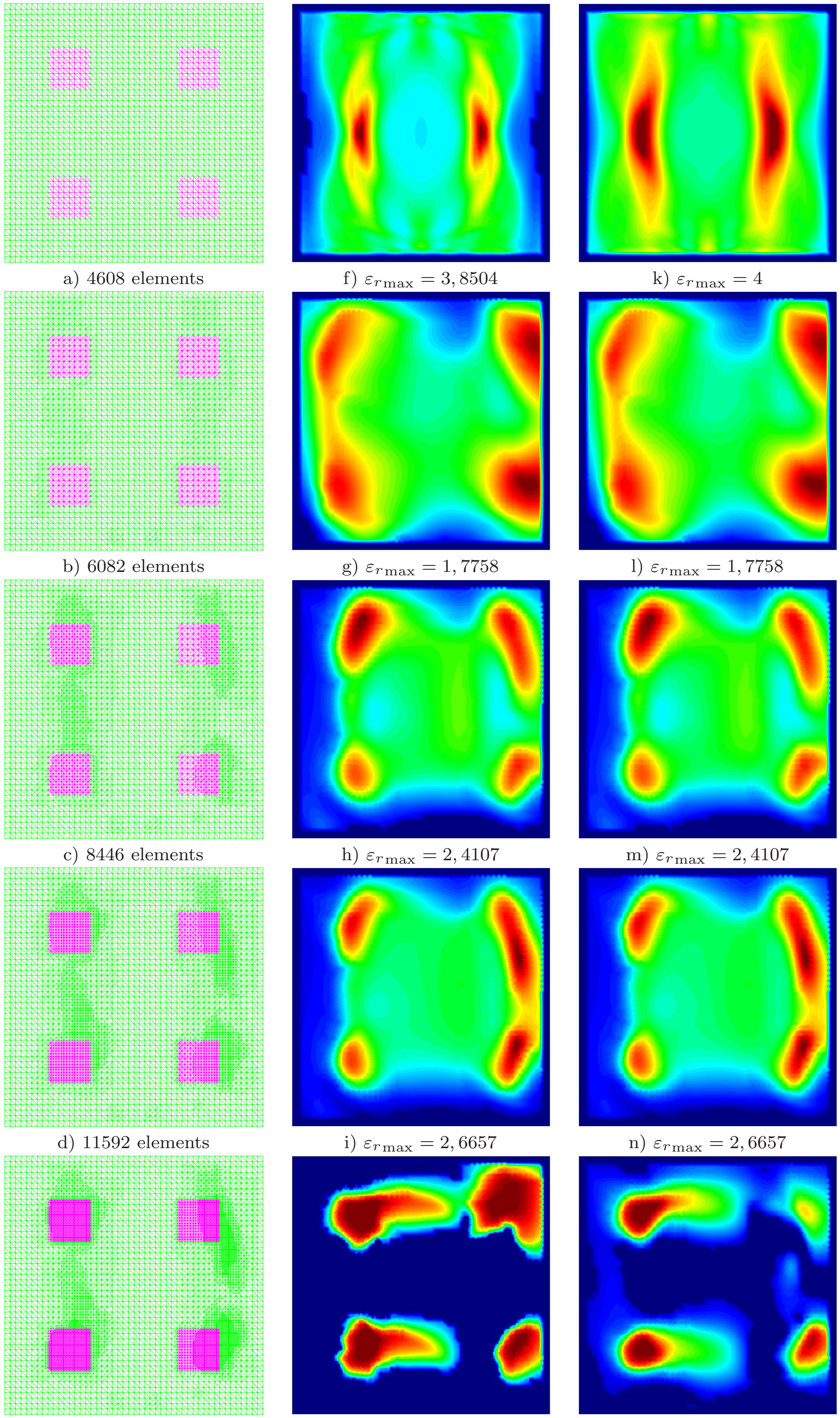

a) 4608 elements | f) $\varepsilon_{r\max} = 3,8504$ | k) $\varepsilon_{r\max} = 4$

b) 6082 elements | g) $\varepsilon_{r\max} = 1,7758$ | l) $\varepsilon_{r\max} = 1,7758$

c) 8446 elements | h) $\varepsilon_{r\max} = 2,4107$ | m) $\varepsilon_{r\max} = 2,4107$

d) 11592 elements | i) $\varepsilon_{r\max} = 2,6657$ | n) $\varepsilon_{r\max} = 2,6657$

e) 16862 elements | j) $\varepsilon_{r\max} = 3,9996$ | o) $\varepsilon_{r\max} = 3,9945$

Figure 7: Example 2: a), b), c), d), e) The adaptively refined meshes for tests with initial guess $\epsilon_{r0} = 1.5$ and $\sigma = 0\%$. f), g), h), i), j) The spatial distribution of the reconstructed function ε_r^m on the coarse mesh and on the first, second, third and fourth adaptively refined meshes when $\epsilon_{r0} = 1.5$ and $\sigma = 0\%$. k), l), m), n), o) The spatial distribution of the reconstructed function ε_r^m on the coarse mesh and on the first, second, third and fourth adaptively refined meshes when $\epsilon_{r0} = 1.5$ and $\sigma = 5\%$.

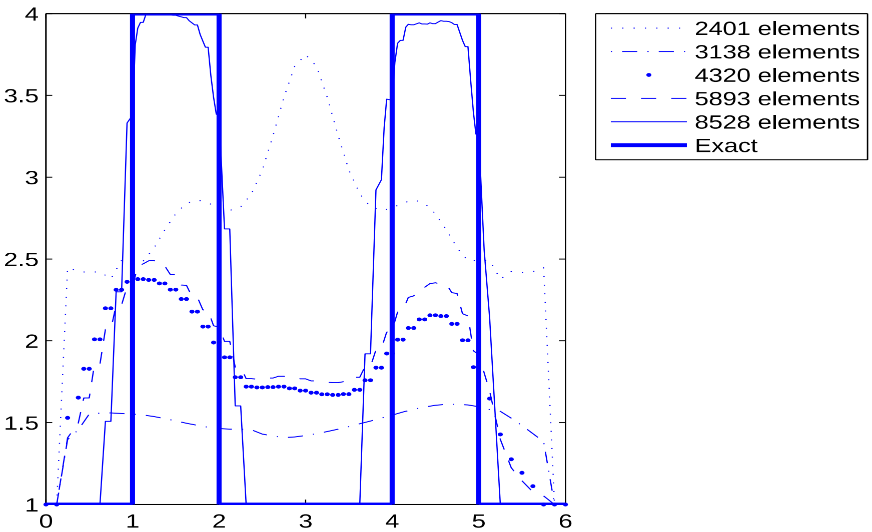

Figure 8: Example 2: the one-dimensional cross-sections of the image of the function $\varepsilon_{r h}^{\ m}$ along the vertical line connecting the points (-1.5,-3.0) and (-1.5,3.0) computed for the corresponding refined meshes with noise level $\sigma = 0\%$ in the data.

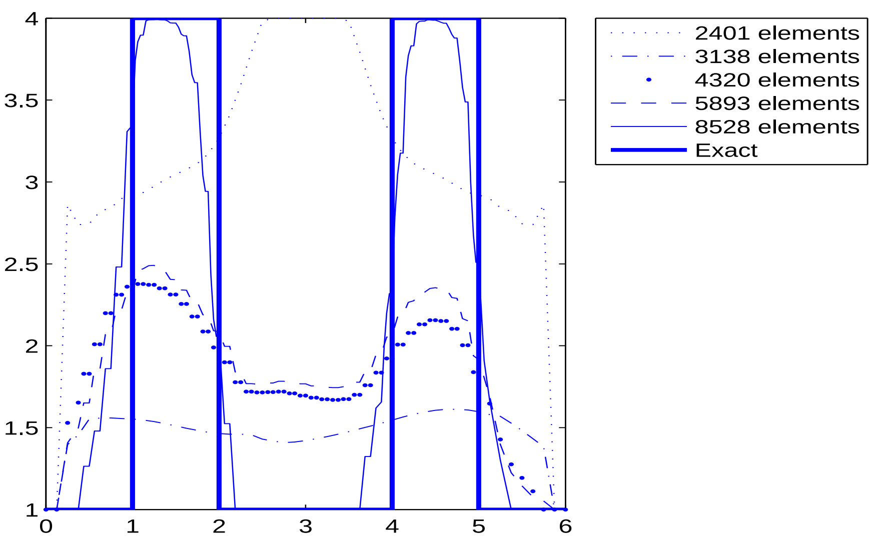

Figure 9: Example 2: the one-dimensional cross-sections of the image of the function $\varepsilon_{r h}^{\ m}$ along the vertical line connecting the points (-1.5,-3.0) and (-1.5,3.0) computed for the corresponding refined meshes with noise level $\sigma = 5\%$ in the data.

9 Conclusions

We have formulated an adaptive FE/FD method for reconstruction of the dielectric function in a symmetric structure. A time limited plane wave is used to generate backscattering data. The adaptivity is based on an *a posteriori* error estimate for the Lagrangian. The mesh is refined in all subdomains of the computational domain where the Fréchet derivative of the Lagrangian attains its maximal values.

Summing up our numerical studies, we can conclude that using the adaptive algorithm of Section 7.1 can significantly improve the location and contrast of the reconstructed dielectric function. At the same time Example 2 shows that the quasi-Newton method converges to the exact solution when a good approximation to the exact solution is available. However, this method deteriorates when a good initial guess is unavailable.

Acknowledgments: The research was partially supported by the Swedish Foundation for Strategic Research (SSF) in Gothenburg Mathematical Modelling Centre (GMMC) and by the Swedish Institute, Visby Program.

References

[1] M. P. H. Andresen, H. E. Krogstad and J. Skaar, *Inverse scattering of two-dimensional photonic structures by layer stripping*, *J. Opt. Soc. Am. B*, 28, 689–696, 2011.

[2] A.B. Bakushinsky, *A posteriori* error estimates for approximate solutions of irregular operator equations, *Doklady Mathematics*, 83, 1–2, 2011.

[3] A.B. Bakushinsky and M.Yu. Kokurin, *Iterative Methods for Approximate Solution of Inverse Problems*, Springer, New York, 2004.

[4] L. Beilina, K. Samuelsson and K. Åhlander, Efficiency of a hybrid method for the wave equation. In *International Conference on Finite Element Methods*, Gakuto International Series Mathematical Sciences and Applications. Gakkotosho CO., LTD, 2001.

[5] L. Beilina and C. Johnson, A hybrid FEM/FDM method for an inverse scattering problem. In *Numerical Mathematics and Advanced Applications - ENUMATH 2001*, Springer-Verlag, Berlin, 2001.

[6] L. Beilina, Adaptive hybrid FEM/FDM methods for inverse scattering problems, *J. Inverse Problems and Information Technologies* , 1, 73–116, 2002.

[7] L. Beilina, Adaptive finite element/difference method for inverse elastic scattering waves, *Applied and Computational Mathematics*, 1, 158–174, 2002.

[8] L. Beilina and C. Johnson, *A posteriori* error estimation in computational inverse scattering, *Mathematical Models and Methods in Applied Sciences*, 15, 23–37, 2005.

[9] L. Beilina and C. Clason, An adaptive hybrid FEM/FDM method for an inverse scattering problem in scanning acoustic microscopy, *SIAM J. Sci. Comp.,* 28, 382–402, 2006.

[10] L. Beilina and M.V. Klibanov, A globally convergent numerical method for a coefficient inverse problem, *SIAM J. Sci. Comp.,* 31, 478–509, 2008.

[11] L. Beilina, M. Hatlo and H. Krogstad, Adaptive algorithm for an inverse electromagnetic scattering problem, *Applicable Analysis*, 1, 15–28, 2009.

[12] L. Beilina and M.V. Klibanov, *A posteriori* error estimates for the adaptivity technique for the Tikhonov functional and global convergence for a coefficient inverse problem, *Inverse Problems,* 26**,** 045012, 2010.

[13] L. Beilina, M. V. Klibanov and A. Kuzhuget, New a posteriori error estimates for adaptivity technique and global convergence for a hyperbolic coefficient inverse problem, *Journal of Mathematical Sciences,* 172, 449–476, 2011.

[14] L.Beilina and M.V.Klibanov, Reconstruction of dielectrics from experimental data via a hybrid globally convergent/adaptive inverse algorithm, *Inverse Problems*, 26, 125009, 2010.

[15] L. Beilina, M.V. Klibanov and M.Yu Kokurin, Adaptivity with relaxation for ill-posed problems and global convergence for a coefficient inverse problem, *Journal of Mathematical Sciences,* 167, 279–325, 2010.

[16] M. Cheney and D. Isaacson, Inverse problems for a perturbed dissipative half-space, *Inverse Problems*, 11, 865- 888, 1995.

[17] G. C. Cohen, *High order numerical methods for transient wave equations*, Springer-Verlag, 2002.

[18] B. Engquist and A. Majda, Absorbing boundary conditions for the numerical simulation of waves *Math. Comp.* 31, 629-651, 1977.

[19] K. Eriksson, D. Estep and C. Johnson, *Calculus in Several Dimensions*, Springer, Berlin, 2004.

[20] M. V. Klibanov, M. A. Fiddy, L. Beilina, N. Pantong and J. Schenk, Picosecond scale experimental verification of a globally convergent numerical method for a coefficient inverse problem, *Inverse Problems*, 26, 045003, 2010.

[21] O. A. Ladyzhenskaya, *Boundary Value Problems of Mathematical Physics*, Springer Verlag, Berlin, 1985.

[22] J. Nocedal, Updating quasi-Newton matrices with limited storage, *Mathematics of Comp.*, V.35, N.151, 773–782, 1991.